

Atomic structure and properties of a perovskite/spinel (111) interfaceYuanmin Zhu,¹ Linhan Liu,¹ Guoping Cao,¹ Wandong Xing,¹ Ying-Hao Chu,² Jing Zhu,¹ and Rong Yu^{1,*}¹*National Center for Electron Microscopy in Beijing, Key Laboratory of Advanced Materials (MOE),
The State Key Laboratory of New Ceramics and Fine Processing, School of Materials Science and Engineering,
Tsinghua University, Beijing 100084, People's Republic of China*²*Department of Materials Science and Engineering, National Chiao Tung University, Hsinchu 30010, Taiwan, Republic of China*

(Received 21 March 2020; revised 7 September 2020; accepted 10 September 2020; published 1 October 2020)

Perovskite and spinel structures are widely found in ferroelectric and magnetic oxides, respectively, making their combination important for multiferroic composites. In this study, the (111) interface between perovskite-type BiFeO₃ and spinel-type NiFe₂O₄, has been systematically investigated at the atomic scale combining aberration-corrected scanning transmission electron microscopy and first-principles calculations. The atomic terminations at the interface were determined to be the BiO₃ layer on the BiFeO₃ side and the tetrahedral Fe layer on the NiFe₂O₄ side. The lattice mismatch between BiFeO₃ and NiFe₂O₄ is primarily accommodated by the first and second BiO₃ layers inside BiFeO₃, indicating a stand-off of misfit dislocations in BiFeO₃. A metallic interface is formed between the two insulating phases, with the BiO₃ and tetrahedral Fe layer coupled antiferromagnetically across the interface. The magnetic moment in NiFe₂O₄ and the ferroelectric polarization in BiFeO₃ drop slightly at the interface and return to the bulk values within two atomic layers from the interface.

DOI: [10.1103/PhysRevB.102.165302](https://doi.org/10.1103/PhysRevB.102.165302)**I. INTRODUCTION**

Interfaces of complex oxides have rich physical properties derived from the interplay of structural, electronic, and magnetic degrees of freedom, which have provided tremendous opportunities for designing and manipulating the next-generation multifunctional devices [1–4]. Heterostructures in complex oxides have provided an integrated platform to study the electrical transport, magnetism, optical response, thermal conductivity, and superconductivity of interfaces [5–7]. Especially, plentiful heterointerfaces exist in nanocomposite film systems with the combination forms of componential phases, such as epitaxial multilayers, nanodots and nanoplates embedded films, and nanocolumnars (3D) embedded heterostructures [8–12].

The physical property of an oxide interface depends sensitively on their atomic arrangements and electronic configurations. For example, the emergence of two-dimensional electron gas and the interface superconductivity at the LaAlO₃/SrTiO₃ interface is controlled by atomic termination of the two phases at the interface [13–15]. The aberration-corrected transmission electron microscopy (TEM), which has proven to be a powerful tool to explore fine structures and chemical information in oxide materials [16,17], has already enabled the atomic-scale observation of the two-dimensional atomically epitaxial superstructures at interfaces like LaAlO₃/La_{0.5}Zr_{0.5}O_{1.75}, YBa₂Cu₃O₇/SrTiO₃, and BiFeO₃/La_{0.67}Sr_{0.33}MnO₃, etc. [18–21].

Among all proposed systems, the perovskite-spinel interface has attracted considerable interests as an oxide-based

magnetic tunnel junction since researches illustrated the importance of the self-assembled epitaxial interface in obtaining large magnetoelectric and magnetoresistance effects [22–24]. Spinel structure is a complex but important one [25–27] widely found in materials for catalysis and magnetism. Perovskite materials have been receiving growing attention due to their applications in multiferroics, catalysis, photovoltaics, solar cell, etc. [28–30]. As demonstrated, the {111} interface is the most popular interface in the self-assembled perovskite-spinel structures due to the minimization of interface energy [22,31]. Although substantial investigations have been performed for perovskite-spinel composites, the interfaces between them are still not well understood.

Taking a typical spinel-perovskite NiFe₂O₄-BiFeO₃ (NFO-BFO) nanocomposite film as a model system, here we analyze the atomic and electronic structures, magnetism, and electric polarization of the interface combining aberration-corrected transmission electron microscopy at atomic resolution and density-functional theory (DFT) calculations.

II. EXPERIMENTAL DETAILS

The nanocomposite BiFeO₃-NiFe₂O₄ thin films were grown on (001)-SrTiO₃ single-crystal substrates with a KrF ($\lambda = 248$ nm) excimer laser by pulsed laser deposition using a single ceramic target with molar ratio of 0.67BaFeO₃-0.33NiFe₂O₄. The substrate was heated to 700 °C, and a dynamic O₂ pressure of ~ 100 mTorr in the chamber was maintained during deposition.

Cross-section samples for scanning transmission electron microscopy (STEM) study were prepared with the Zeiss Auriga focused ion beam system. Aberration-corrected STEM measurements were performed by a double-corrected TEM

*ryu@tsinghua.edu.cn

(Titan Themis 60-300), equipped with a high-brightness Schottky emitter (XFEG) and a Gatan Quantum 965 spectrometer. The high-angle annular dark-field (HAADF) images were acquired at 300 kV, where the probe size was about 1 Å and the convergence angle was confined at 25 mrad. The collection angle for HAADF images was 64–200 mrad. STEM technique combined with HAADF imaging and annular bright-field (ABF) imaging is a powerful tool for the investigation of the atomic structure of various materials containing both heavy and light elements. The contrast of HAADF image exhibits a $Z^{1.7}$ dependency in heavy elements imaging, where Z represents the atomic number [32]. To reduce the noise, most HAADF images were recorded for 4 s using a continuous-acquiring mode with 0.4 s per frame, resulting in 10 frames per image which were aligned and added together.

Electron-energy-loss spectroscopy (EELS) spectra were acquired with dual-EELS mode. The exposure time of each pixel was 0.5 s, with a total time for each line-scan spectrum of approximately 2 min. For calculation of the $L_{3,2}$ ratios, the statistical intensities are integrated over 3.5–4-eV windows centered on the peak of the corresponding $L_{3,2}$ edges. All the EELS spectra were processed using the DIGITALMICROGRAPH v3.0 software.

III. THEORETICAL DETAILS

Calculations based on DFT were performed using the projector-augmented wave method, as implemented in the Vienna *Ab initio* Simulation Package (VASP) [33–35]. The generalized gradient approximation + U method was used to describe the exchange-correlation function, and the effective U energies for Fe and Ni elements are set as 4 and 2 eV, respectively, following previous studies [36–38]. The plane-wave cutoff energy was set to 450 eV. Integrations over the Brillouin zone were performed using a Monkhorst-Pack grid of $5 \times 3 \times 1$. The k -point sampling in the Brillouin zone and the plane-wave cutoff energy were tested to ensure that the total energies converged to 1 meV per atom. The structural relaxations were performed until the residual forces were less than 0.05 eV/Å.

The slab size for NFO or BFO (111) plane was selected to be suitable to connect to each other with the size of about $u = 5.77$ Å, $v = 10.06$ Å. To keep the periodic of the supercell, the oxygen arrangement should follow a close-packed fcc sublattice at the (111) interface along the c direction, in which 8 oxygen layers in NFO slab and 10 oxygen layers in BFO slab were carefully selected to build the supercell. The supercell model contains 208 atoms with the lattice of 5.769 Å \times 10.0557 Å \times 41.206 Å, $\alpha = \beta = \gamma = 90^\circ$ (42 atomic layers), as shown in Fig. S2 in detail (see Supplemental Material [39]). Lattice parameters and atomic positions combined with the magnetic moments were optimized simultaneously.

IV. RESULTS AND DISCUSSION

Spinel oxides can be described by the general formula AB_2O_4 , where A and B stand for tetrahedral and octahedral cation sites in a close-packed fcc sublattice of oxygen. $NiFe_2O_4$ is a well-known inverse spinel, which can be written

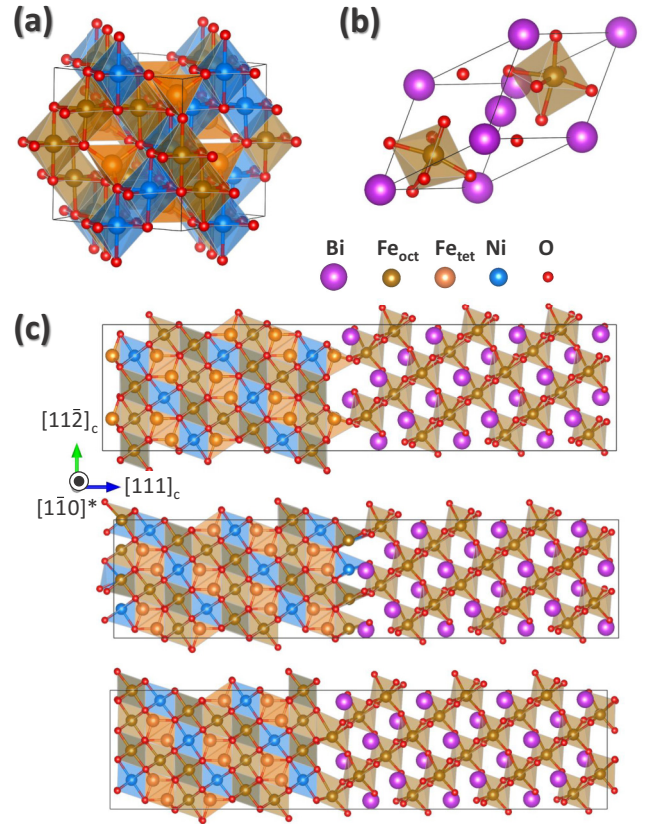


FIG. 1. The structures and interface types of the material system. (a) Schematic cubic unit cell of the inverse spinel $NiFe_2O_4$ (space group $Fd\bar{3}m$). The octahedral sites are occupied by nickel (blue) and iron (golden) atoms while the tetrahedral sites are occupied by iron (orange) atoms. The Fe_{tet} , Fe_{oct} refer to iron atoms on the tetrahedral site and octahedral sites, respectively. (b) Schematic rhombohedral unit cell of $BiFeO_3$. The large purple and small red balls stand for the bismuth and oxygen atoms, respectively. (c) Three types of interface models, i.e., NFO-(Fe^{3+})/[BiO_3]³⁻-BFO (Fig. S2 in detail; see Supplemental Material [39]), NFO-[Ni, Fe]₃^{7.5+}/[BiO_3]³⁻-BFO, NFO-/[Fe]³⁺-BFO from the top to the bottom.

as $(Fe^{3+})[Ni^{2+}, Fe^{3+}]O_4$, with Ni^{2+} ions on B sites and Fe^{3+} ions occupying equally A and B sites. For clarity, the parentheses and brackets refer to tetrahedral and octahedral sites, respectively. As schematically shown in Fig. 1(a), the conventional cubic unit cell of $NiFe_2O_4$ contains eight formula units (space group $Fd\bar{3}m$). The stacking sequence of the (111) plane of $NiFe_2O_4$ can be described as O_4^{8-} -[Ni, Fe]₃^{7.5+}- O_4^{8-} -(Fe)³⁺-[Ni, Fe]₂^{2.5+}-(Fe)³⁺, where the superscripts denote the nominal charges. There are six types of possible (111) surface layers in the NFO phase [shown in Fig. S1(a); see Supplemental Material [39]]. Figure 1(b) shows the rhombohedral unit cell of $BiFeO_3$, which has the space group $R3c$ with atoms distorted from the ideal cubic perovskite structure. The following indexing for BFO was referred to the so-called pseudocubic structure for simplicity, with the pseudocubic lattice parameter of $a_{pc} = 3.96$ Å. There are only two types of (111) terminations in $BiFeO_3$, i.e., [BiO_3]³⁻ and [Fe]³⁺ layers [shown in Fig. S1(b); see Supplemental

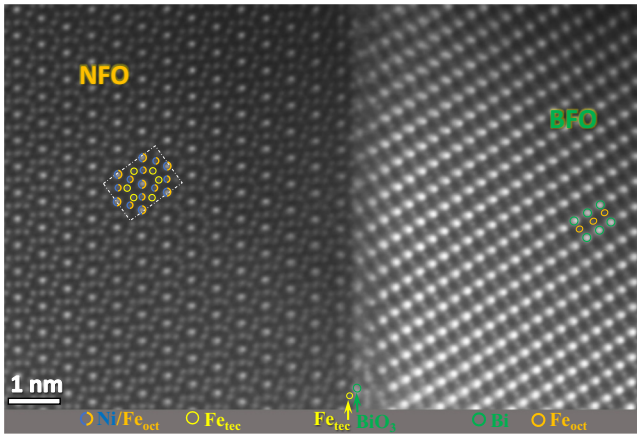


FIG. 2. A high-resolution HAADF images of the BFO-NFO(111) interface. The atomic configuration of the interface can be identified to be NFO-(Fe)³⁺/[BiO₃]³⁻-BFO.

Material [39]). Considering the charge balance at the interface, we built three types of BFO-NFO (111) interface models for different NFO and BFO surface terminations, i.e., NFO-(Fe)³⁺/[BiO₃]³⁻-BFO, NFO-[Ni, Fe]₃^{7,5+}/[BiO₃]³⁻-BFO, NFO O₄⁸⁻/[Fe]³⁺-BFO, as shown in Fig. 1(c). To identify and understand the real interface structure, detailed high-resolution TEM analysis combined with DFT calculations were performed.

Figure 2 shows a typical HAADF image of the NFO-BFO (111) interface, viewed along the $[1\bar{1}0]_c$ direction. Low-magnification morphologies of nanocomposite NFO-BFO films and more examples of the (111) interface can be found in the supporting materials (Figs. S3 and S4; see Supplemental Material [39]). The unit cell of NFO projected along the $[1\bar{1}0]_c$ direction is outlined with blue rectangles. The Ni, Fe, Bi columns are clearly resolved in the image. The atomic layers at the interface can be directly identified to be the tetrahedral (Fe)³⁺ at the NFO side and the [BiO₃]³⁻ at the BFO side, respectively, consistent with the NFO-(Fe)³⁺/[BiO₃]³⁻-BFO shown in Fig. 1(c) (top). As in the bulk, the interface (Fe)³⁺ atoms stay in tetrahedra formed by oxygen in NFO and BFO across the interface. The interface FeO₄ tetrahedra share corners with the FeO₆ octahedra in BFO.

According to the bulk lattice parameters, the lattice misfit between BFO and NFO is about 6.2%. The mechanism to accommodate the misfit strain is important to understand the strain state of BFO and NFO near the interface. Figure 3(a) shows misfit dislocations at the interface. Firstly, the atomic center positions were determined by fitting the bright spots in the image with 2D Gaussian function as introduced in Ref. [40]. The displacements of the atomic columns from the periodic lattices are shown as vectors overlapping on the image (yellow arrows in NFO and red ones in BFO). As we can see, there are negligible displacements in NFO, but remarkable displacements in BFO phase, demonstrating that the BFO lattice at the interface are obvious different with its bulk lattice. An extra half plane is observed for every 15 lattice planes in BFO, corresponding to a misfit of $\sim 6.6\%$. It means that the lattice misfit between NFO and BFO is primarily accommodated by the strain in BFO.

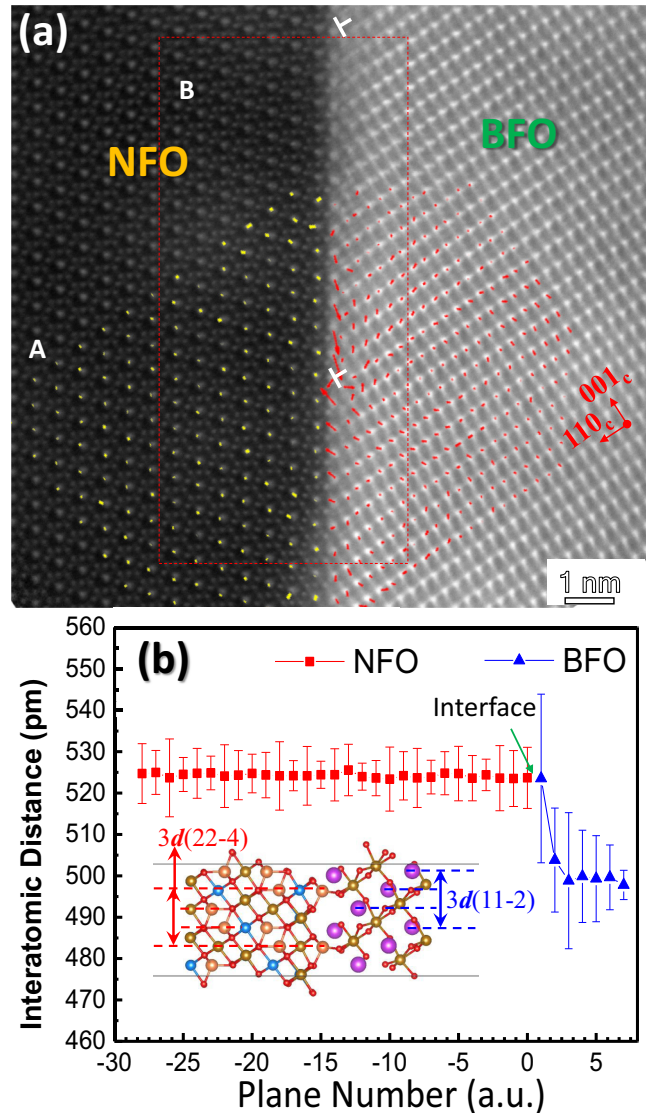


FIG. 3. Strain analysis at the BFO-NFO (111) interface. (a) A HAADF image of the BFO-NFO(111) interface showing misfit dislocations and the displacements of the atomic columns overlapping on the HAADF image. (b) The interatomic distance parallel to the interface. The interface is located at plane number 0.

Another feature of the interface is the one-to-one correspondence (zero misfit) between the atomic columns in NFO and those in the first BiO₃ layer in BFO. We measured the in-plane interatomic distances, as shown in Fig. 3(b). In NFO, the Fe-Fe (or Ni) distance is about 5.2 ± 0.1 Å at the interface and inside the bulk. In BFO, the Bi-Bi distance in the first layer (plane number 1) is stretched to ~ 5.2 Å, which is the same as the value in NFO. The perfect registry between the first layers in NFO and BFO suggests a strong bonding at the interface, making the first BiO₃ layer highly strained. Furthermore, GPA analysis of the (111)BFO-NFO interface also can demonstrate a strained layer of BFO existing at the interface (shown in Fig. S5; see Supplemental Material [39]).

In BFO, the in-plane Bi-Bi distance went down sharply to ~ 5.03 Å in the second layer (slightly stretched) and

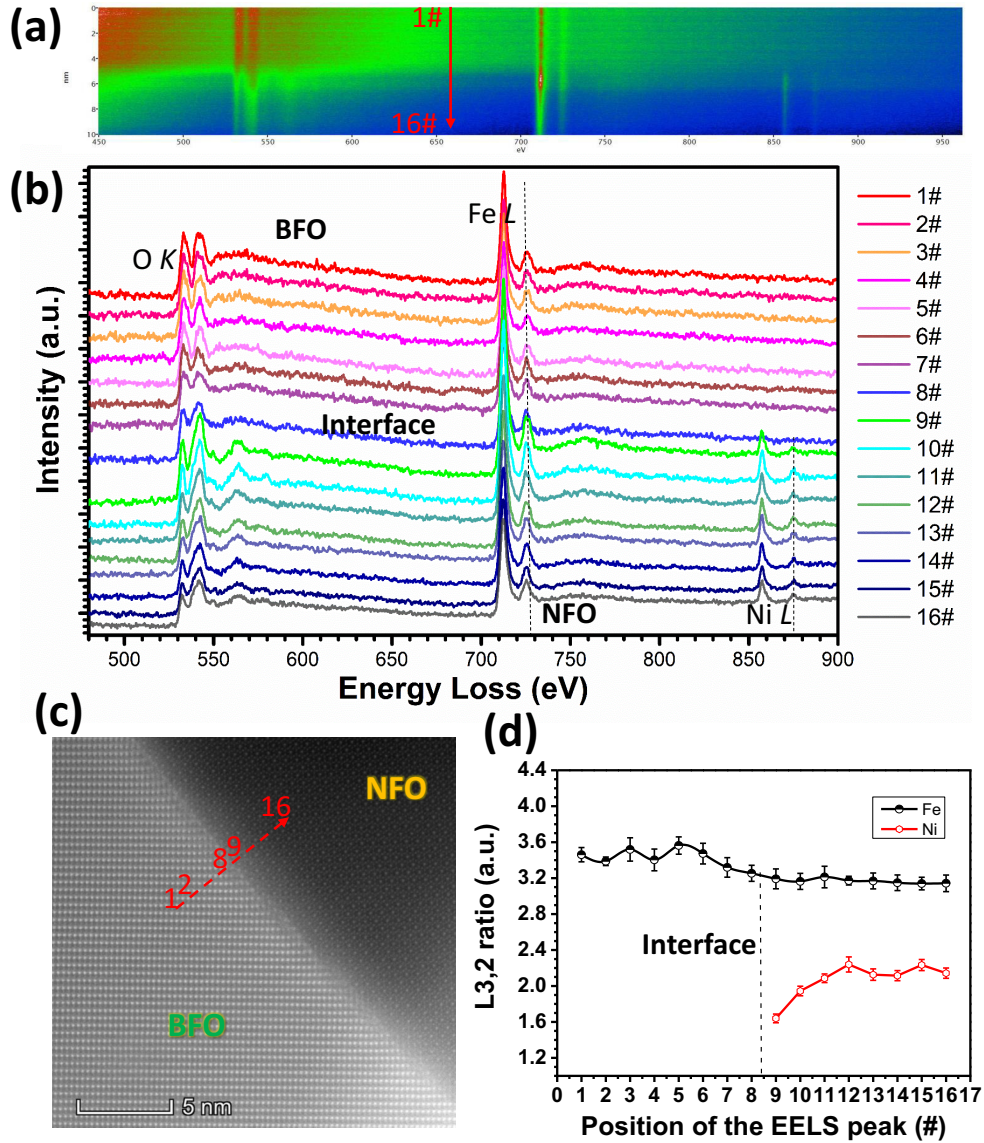


FIG. 4. EELS results for the NFO-BFO (111) interface. (a) EELS spectrum image of the acquisition line scan across the NFO-BFO (111) interface. (b) Series of EELS signals for the Fe, Ni L edges and O K edge extracted from (a). (c) The corresponding HAADF image showing the STEM-EELS acquiring positions with a red dashed arrow. (d) $L_{3,2}$ ratios calculated from the Fe, Ni L edges. The statistical intensities are integrated over 3.5–4-eV windows centered on the peak of the $L_{3,2}$ edges.

remained ~ 4.98 Å (the bulk value) for the rest, indicating that the lattice misfit exists only between the first BiO_3 layer and the remaining BFO lattice. In general, elastic interaction between the component phases plays a key role in the formation of the interfaces in epitaxial nanocomposite thin films [41,42]. Both theoretical and experimental results reveal that the Young modulus of NFO material is about 189.4 GPa, which is much larger than that of the BFO phase (~ 85 GPa) [43,44]. Therefore, when NFO meets BFO in the self-assembled perovskite-spinel heterostructures, the relatively soft BFO is strained to accommodate the misfit so as to lower the strain energy, leading to the formation of so-called “stand-off” [45,46] dislocations only in BFO, leaving NFO in an unstrained state.

To investigate the nature of the oxidation state at the interface, line-scan profiles of electron-energy-loss spectroscopy across the $\{111\}_{\text{BFO/NFO}}$ planes were carefully performed. One set of the images and corresponding EELS spectra are given in Fig. 4. Series of EELS signals for the O K and Fe, Ni L edges are shown in Fig. 4(b) extracted from the corresponding spectrum image of Fig. 4(a) and the acquiring positions of the line scan were indicated by a red dotted arrow in the STEM-HAADF image [Fig. 4(c)]. As shown in the O K edges, the electron-energy-loss peak I at ~ 535 eV has the similar maximum intensity with the peak at ~ 542 eV in BFO phase, representing the Fe-O hybridization [47], while in the NFO phase the intensity of energy-loss peak at ~ 535 eV is obviously lower than that of the peak at ~ 542 eV and

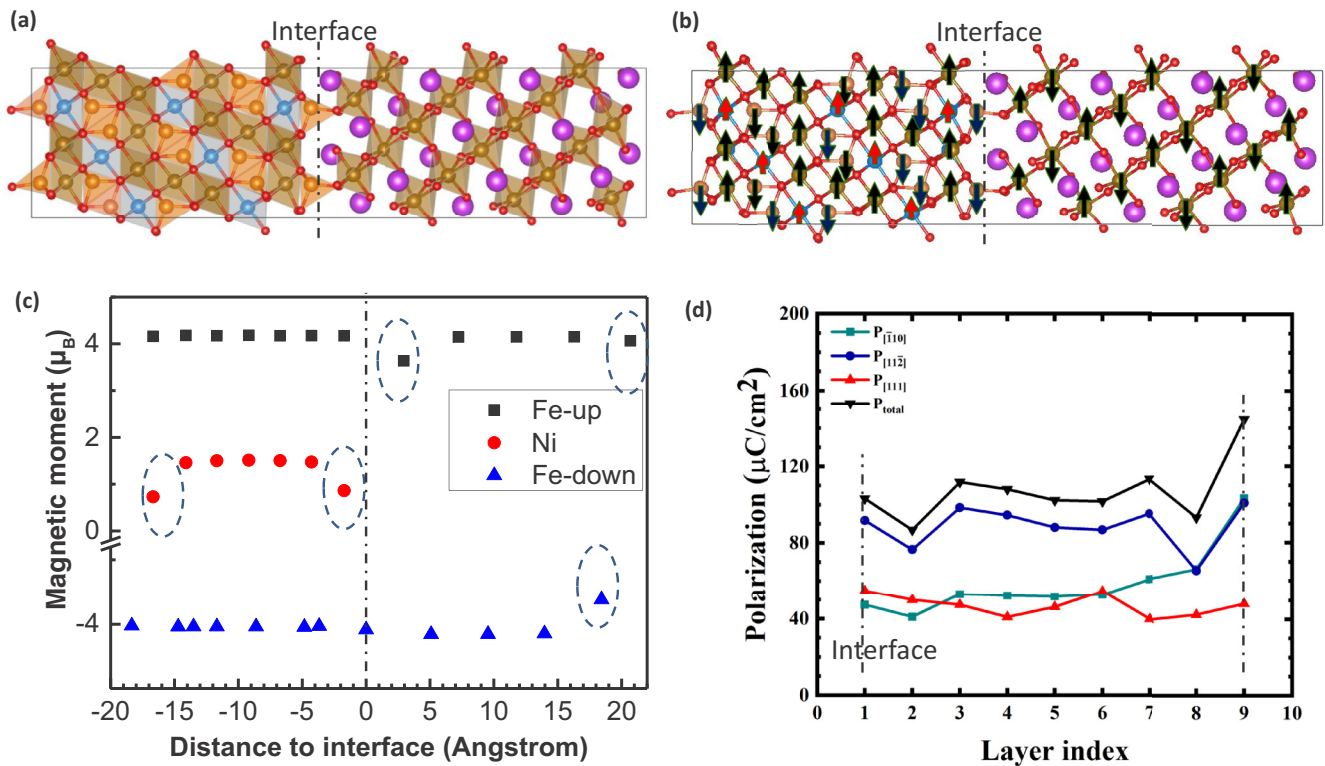


FIG. 5. Atomic structure and magnetic configuration of the NFO-BFO (111) interface. (a) The final relaxed structure of the interface using DFT calculations. (b) The magnetic configuration with AFM coupling at the interface. (c) The magnetic moments across the interface. The first tetrahedral Fe^{3+} at the NFO side is set at 0. (d) Calculated ferroelectric polarization of BFO based on Born effective charge method.

an additional peak at ~ 564 eV exists. It shows that the O K -edge signals in NFO phase have multiple signals of the Ni-O hybridization [48] and Fe-O interaction. Specially, the EELS 8#, which is just from the BFO-NFO interface, displays a distinct feature that is different from the ones in the BFO and NFO bulk phase. In the Fe L edge, there is a chemical shift of ~ 1 eV to low-energy loss from the BFO phase to NFO, illustrating a decreasing of the oxidation state of Fe ion. There is also a chemical shift to low energy for the Ni L edge from the NFO bulk to the interface. Furthermore, we calculated the $L3/2$ ratios of the Fe, Ni EELS signals by the integrated intensity at the peak and the results are shown in Fig. 4(d). The $L3/2$ ratio of Fe EELS decreases from the BFO (Fe^{3+}) to NFO phase, demonstrating the Fe ion in the NFO phase has a mixed oxidation state of Fe^{3+} and Fe^{2+} rather than the nominal Fe^{3+} state, which coincides with the point of view of previous literature [25–27]. An intermediate state of Fe ion was observed at the interface, illustrating a slight increasing of the oxidation state in tetrahedral (Fe-O)/NFO interface layer. The $L3/2$ ratio of Ni decreases from the NFO bulk to the interface layer, meaning a decreasing of oxidation state for Ni ions. Therefore, we found the synergetic variations of oxidation states of Fe, Ni elements from their core-loss EELS spectra and also the O K edges at the (111) NFO-BFO interface.

To understand the structural, electronic, and magnetic properties of the interface, the structure model determined based on the TEM experiments, i.e., the

NFO- $(\text{Fe}^{3+})/[\text{BiO}_3]^{3-}$ -BFO, were further optimized using first-principle calculations. The other models were relaxed to distinct structures from the experimental ones and are not considered in the following. In the calculations, the initial magnetic configurations inside NFO and BFO were set according to the corresponding bulk ones, i.e., ferrimagnetic configuration in NFO and antiferromagnetic (AFM) configuration in BFO. The magnetic coupling across the interface could be either ferromagnetic or antiferromagnetic. Both configurations were considered in the calculations.

The optimized BFO-NFO (111) atomic structure with AFM coupling is given in Fig. 5(a). As can be seen, the FeO_4 tetrahedra in NFO connect the FeO_6 octahedra in BFO at the interface, confirming the experimental observations. The interface with AFM coupling [magnetic configuration shown in Fig. 5(b)] has lower energy than that of the FM coupling. Also, the calculated interface energy based on our DFT calculation results demonstrate that the interface with AFM coupling configuration has lower interface energy (details in Figs. S8 and S9; see Supplemental Material [39]). The magnetic moments of each (111) layer in the heterostructures are given in Fig. 5(c). The magnetic moments of Ni and Fe atoms decrease obviously at the interface (marked by the dotted circles) illustrating the changes of their electronic structures, which is related to the EELS analysis of the variations of oxidation states of Fe, Ni elements.

In order to discuss the interface effect on the ferroelectricity of BFO, we calculated ferroelectric polarization

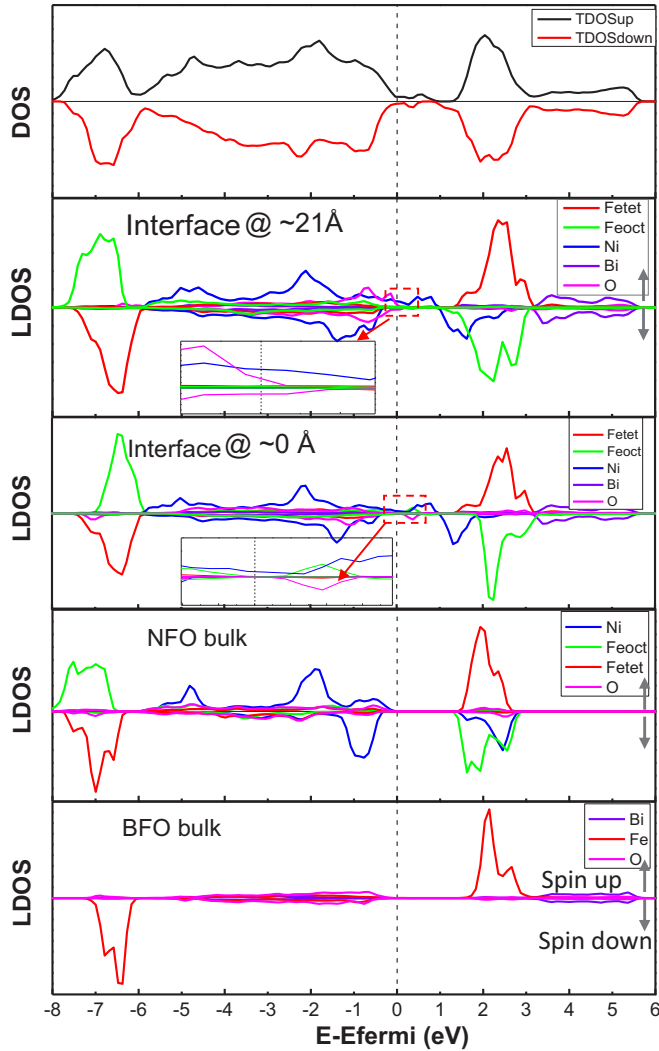


FIG. 6. Total and local densities of states of the BFO-NFO (111) interfaces and bulk phases.

in BFO using Born effective charges [49,50]. It should be noted that both BiFeO_3 and NiFe_2O_4 have threefold symmetry in the [111] direction, making it possible to estimate the polarization close to the (111) interface using Born effective charges derived for the [111] polarization direction. In the light of the definition of dimensionless Born charge $Z_{s,\alpha\beta}^*$, the polarization induced by atomic displacement can be written as

$$P_\alpha = Z_{s,\alpha\beta}^* \frac{e}{\Omega} u_{s,\beta}, \quad (1)$$

where e is the charge quantum, Ω is the volume of unit cell, $u_{s,\beta}$ is the displacement of ion s in the direction of β , which is obtained by comparing the relaxed BFO structure with the undistorted perovskite structure ($Pm\bar{3}m$ symmetry, as usually adopted in literature on BiFeO_3) as the centrosymmetric reference. The Born effective charges for each type of element here were set as $Z_{\text{Bi}}^* = 4.37$, $Z_{\text{Fe}}^* = 3.49$, $Z_{\text{O}}^* = -2.62$ [50]. The calculated polarization along each direction of the Cartesian coordinate is shown in Fig. 5(d). As the lattice mismatch is mainly limited to the first two layers near the interface, the ferroelectric polarization has obvious fluctuations in these

layers, and then its value tends to grow back to a steady state at the central region of BFO. Interestingly, the ferroelectric polarization in (111) plane (red) is slightly decreased from the interface (layer 1 and 9) to BFO bulk and the similar results of the ferroelectric displacement mapping at the (111) interface are observed from the quantitative measurements of the high-resolution STEM image (Fig. S6; see Supplemental Material [39]).

Electronic structure is important to reveal electronic and magnetic properties of the interface. Figure 6 gives the densities of states (DOS) with spin up and -down projected onto different layers of the interface model. The labels marked “NFO bulk” and “BFO bulk” mean the projections on the layers far from the interface, where the bonding environment is almost identical to that in the corresponding bulk materials. The DOS curves are similar to the previous DFT calculations for the NFO and BFO bulk materials [51,52]. The calculated energy band gap of bulk NFO and BFO is ~ 1.55 and 2.30 eV, respectively. It is also comparable to the experimental results of optical band gap for NFO (~ 1.6 eV) and BFO (~ 2.5 eV) materials, respectively [53,54].

It is interesting to note that there are electronic states at the Fermi level for the spin-up component and (to a lesser extent) for the spin-down component, indicating that the interface is metallic and spin polarized. In particular, the electronic states at the interface are primarily associated with the Ni^{2+} , O^{2-} ions (shown in the insets of the local densities of states (LDOS) of interfaces). The current calculation results show that the BFO-NFO (111) interface is more conductive than the bulk, consistent with previous experimental results about local conductive interfaces in perovskite-spinel films [55].

V. CONCLUSION

In summary, the atomic structure and properties of the (111) interface between NiFe_2O_4 and BiFeO_3 phases have been investigated using the aberration-corrected high resolution scanning transmission electron microscopy (HRSTEM) and first-principles calculations. The atomic structure was determined to be $\text{NFO}(111)\text{-(Fe)}^{3+}/\{\text{BiO}_3\}^{3-}\text{-BFO}(111)$. Quantitative measurement of the atomic positions at the (111) interface revealed the stand-off of misfit dislocations for the accommodation of the lattice mismatch between the two phases. The density-functional theory calculations confirmed the experimental atomic structure and revealed an antiferromagnetic coupling across the interface, a metallic character at the interface, and slight drops in magnetism and ferroelectric polarization close to the interface.

ACKNOWLEDGMENTS

This work was supported by Basic Science Center Project of NSFC (Project No. 51788104), National Natural Science Foundation of China (Grants No. 51525102, No. 51761135131, No. 51571021, and No. 11775018). In this work we used the resources of the National Center for Electron Microscopy in Beijing, Shanghai Supercomputer Center, and Tsinghua National Laboratory for Information Science and Technology.

- [1] W. Eerenstein, N. D. Mathur, and J. F. Scott, *Nature (London)* **442**, 759 (2006).
- [2] J. Garcia-Barriocanal, F. Y. Bruno, A. Rivera-Calzada, Z. Sefrioui, N. M. Nemes, M. Garcia-Hernández, J. Rubio-Zuazo, G. R. Castro, M. Varela, S. J. Pennycook, C. Leon, and J. Santamaria, *Adv. Mater.* **22**, 627 (2010).
- [3] C. A. F. Vaz, J. Hoffman, C. H. Ahn, and R. Ramesh, *Adv. Mater.* **22**, 2900 (2010).
- [4] J. Mannhart and D. G. Schlom, *Science* **327**, 1607 (2010).
- [5] H. Kroemer, *Rev. Mod. Phys.* **73**, 783 (2001).
- [6] J. M. Rondinelli and S. J. May, *Nat. Mater.* **11**, 833 (2012).
- [7] J. Chakhalian, A. J. Millis, and J. Rondinelli, *Nat. Mater.* **11**, 92 (2012).
- [8] Y. Z. Chen, N. Bovet, F. Trier, D. V. Christensen, F. M. Qu, N. H. Andersen, T. Kasama, W. Zhang, R. Giraud, J. Dufouleur, T. S. Jespersen, J. R. Sun, A. Smith, J. Nygård, L. Lu, B. Büchner, B. G. Shen, S. Linderoth, and N. Pryds, *Nat. Commun.* **4**, 1371 (2013).
- [9] M. O'Sullivan, J. Hadermann, M. S. Dyer, S. Turner, J. Alaria, T. D. Manning, A. M. Abakumov, J. B. Claridge, and M. J. Rosseinsky, *Nat. Chem.* **8**, 347 (2016).
- [10] J. L. MacManus-Driscoll, S. R. Foltyn, Q. X. Jia, H. Wang, A. Serquis, L. Civale, B. Maiorov, M. E. Hawley, M. P. Maley, and D. E. Peterson, *Nat. Mater.* **3**, 439 (2004).
- [11] H. Zheng, J. Wang, S. E. Lofland, Z. Ma, L. Mohaddes-Ardabili, T. Zhao, L. Salamanca-Riba, S. R. Shinde, S. B. Ogale, F. Bai, D. Viehland, Y. Jia, D. G. Schlom, M. Wuttig, A. Roytburd, and R. Ramesh, *Science* **303**, 661 (2004).
- [12] Y. Zhu, P. Liu, R. Yu, Y.-H. Hsieh, D. Ke, Y.-H. Chu, and Q. Zhan, *Nanoscale* **6**, 5126 (2014).
- [13] M. Basletic, J.-L. Maurice, C. Carrétéro, G. Herranz, O. Copie, M. Bibes, É. Jacquet, K. Bouzehouane, S. Fusil, and A. Barthélémy, *Nat. Mater.* **7**, 621 (2008).
- [14] J. A. Bert, B. Kalisky, C. Bell, M. Kim, Y. Hikita, H. Y. Hwang, and K. A. Moler, *Nat. Phys.* **7**, 767 (2011).
- [15] V. T. Tra, J.-C. Yang, Y.-H. Hsieh, J.-Y. Lin, Y.-C. Chen, and Y.-H. Chu, *Phys. Status Solidi RRL* **8**, 478 (2014).
- [16] R. Yu, L. H. Hu, Z. Y. Cheng, Y. D. Li, H. Q. Ye, and J. Zhu, *Phys. Rev. Lett.* **105**, 226101 (2010).
- [17] Y. Zhang, W. Wang, W. Xing, S. Cheng, S. Deng, M. Angst, C.-P. Yu, F. Lan, Z. Cheng, D. Mandrus, B. Sales, J. Shen, X. Zhong, N.-H. Tai, R. Yu, and J. Zhu, *Phys. Rev. Lett.* **123**, 247601 (2019).
- [18] J. Garcia-Barriocanal, A. M. Perez-Muñoz, Z. Sefrioui, D. Arias, M. Varela, C. Leon, S. J. Pennycook, and J. Santamaria, *Phys. Rev. B* **87**, 245105 (2013).
- [19] Y.-M. Kim, A. Kumar, A. Hatt, A. N. Morozovska, A. Tselev, M. D. Biegalski, I. Ivanov, E. A. Eliseev, S. J. Pennycook, J. M. Rondinelli, S. V. Kalinin, and A. Y. Borisevich, *Adv. Mater.* **25**, 2497 (2013).
- [20] A. B. Shah, Q. M. Ramasse, X. Zhai, J. G. Wen, S. J. May, I. Petrov, A. Bhattacharya, P. Abbamonte, J. N. Eckstein, and J.-M. Zuo, *Adv. Mater.* **22**, 1156 (2010).
- [21] Y. Sun, L. Zhao, H. Pan, X. Lu, L. Gu, Y.-S. Hu, H. Li, M. Armand, Y. Ikuhara, L. Chen, and X. Huang, *Nat. Commun.* **4**, 1870 (2013).
- [22] Z. Tan, J. Slutsker, and A. L. Roytburd, *J. Appl. Phys.* **105**, 061615 (2009).
- [23] Y. Zhu, Q. Zhan, J.-C. Yang, Y. Bitla, P. Liu, C.-I. Li, H.-J. Liu, V. S. Kumar, E. Arenholz, and Q. He, *ACS Appl. Mater. Interfaces* **8**, 1104 (2016).
- [24] J. Ma, J. Hu, Z. Li, and C.-W. Nan, *Adv. Mater.* **23**, 1062 (2011).
- [25] N. Ponpandian, P. Balaya, and A. Narayanasamy, *J. Phys.: Condens. Matter* **14**, 3221 (2002).
- [26] S. C. Petitto, E. M. Marsh, G. A. Carson, and M. A. Langell, *J. Mol. Catal. Chem.* **281**, 49 (2008).
- [27] A. H. Morr and K. Haneda, *J. Appl. Phys.* **52**, 2496 (1981).
- [28] T. Nishimura, A. Ikeda, H. Namba, T. Morishita, and Y. Kido, *Surf. Sci.* **421**, 273 (1999).
- [29] Y. Han, S. Meyer, Y. Dkhissi, K. Weber, J. M. Pringle, U. Bach, L. Spiccia, and Y.-B. Cheng, *J. Mater. Chem. A* **3**, 8139 (2015).
- [30] T. Choi, S. Lee, Y. J. Choi, V. Kiryukhin, and S.-W. Cheong, *Science* **324**, 63 (2009).
- [31] H. Zheng, Q. Zhan, F. Zavaliche, M. Sherburne, F. Straub, M. P. Cruz, L.-Q. Chen, U. Dahmen, and R. Ramesh, *Nano Lett.* **6**, 1401 (2006).
- [32] S. D. Findlay, N. Shibata, H. Sawada, E. Okunishi, Y. Kondo, T. Yamamoto, and Y. Ikuhara, *Appl. Phys. Lett.* **95**, 191913 (2009).
- [33] P. E. Blöchl, *Phys. Rev. B* **50**, 17953 (1994).
- [34] G. Kresse and J. Furthmüller, *Comput. Mater. Sci.* **6**, 15 (1996).
- [35] G. Kresse and J. Furthmüller, *Phys. Rev. B* **54**, 11169 (1996).
- [36] D. Fritsch and C. Ederer, *Phys. Rev. B* **82**, 104117 (2010).
- [37] C. Cheng, *J. Magn. Magn. Mater.* **325**, 144 (2013).
- [38] U.-G. Jong, C.-J. Yu, Y.-S. Park, and C.-S. Ri, *Phys. Lett. A* **380**, 3302 (2016).
- [39] See Supplemental Material at <http://link.aps.org/supplemental/10.1103/PhysRevB.102.165302> for 111-surfaces stacking of BFO and NFO phases, BFO-NFO(111) interface model, low-magnification morphologies of NFO-BFO films, HAADF and ABF images for the (111) interface, GPA analysis of the (111) interface, ferroelectric displacement mapping in the BFO phase and interface energy calculation, which includes Ref. [56].
- [40] C. T. Nelson, B. Winchester, Y. Zhang, S.-J. Kim, A. Melville, C. Adamo, C. M. Folkman, S.-H. Baek, C.-B. Eom, D. G. Schlom, L.-Q. Chen, and X. Pan, *Nano Lett.* **11**, 828 (2011).
- [41] J. L. MacManus-Driscoll, P. Zerrer, H. Wang, H. Yang, J. Yoon, A. Fouchet, R. Yu, M. G. Blamire, and Q. Jia, *Nat. Mater.* **7**, 314 (2008).
- [42] D. G. Schlom, L.-Q. Chen, C. J. Fennie, V. Gopalan, D. A. Muller, X. Pan, R. Ramesh, and R. Uecker, *MRS Bull.* **39**, 118 (2014).
- [43] Z. Li, E. S. Fisher, J. Z. Liu, and M. V. Nevitt, *J. Mater. Sci.* **26**, 2621 (1991).
- [44] S. A. T. Redfern, C. Wang, J. W. Hong, G. Catalan, and J. F. Scott, *J. Phys.: Condens. Matter* **20**, 452205 (2008).
- [45] M. Yu. Gutkin and A. E. Romanov, *Phys. Status Solidi A* **144**, 39 (1994).
- [46] J. Th. M. De Hosson and B. J. Kooi, *Handbook of Surfaces and Interfaces in Materials* (Academic Press, New York, 2001), Vol. 1, Chap. 1, pp. 35–38.
- [47] J. A. Mundy, Q. Mao, C. M. Brooks, D. G. Schlom, and D. A. Muller, *Appl. Phys. Lett.* **101**, 042907 (2012).

- [48] Y. Zhu, C. Li, Q. Wang, J. Wang, L. Chen, and M. Gu, *Appl. Phys. Lett.* **115**, 143902 (2019).
- [49] R. Resta and D. Vanderbilt, *Physics of Ferroelectrics* (Springer, Berlin, 2007), pp. 31–68.
- [50] J. B. Neaton, C. Ederer, U. V. Waghmare, N. A. Spaldin, and K. M. Rabe, *Phys. Rev. B* **71**, 014113 (2005).
- [51] D. Fritsch and C. Ederer, *J. Phys. Conf. Ser.* **292**, 012014 (2011).
- [52] J. Jilili, U. Eckern, and U. Schwingenschlögl, *EPL Europhys. Lett.* **102**, 67009 (2013).
- [53] Q.-C. Sun, H. Sims, D. Mazumdar, J. X. Ma, B. S. Holinsworth, K. R. O’Neal, G. Kim, W. H. Butler, A. Gupta, and J. L. Musfeldt, *Phys. Rev. B* **86**, 205106 (2012).
- [54] F. Gao, Y. Yuan, K. F. Wang, X. Y. Chen, F. Chen, J.-M. Liu, and Z. F. Ren, *Appl. Phys. Lett.* **89**, 102506 (2006).
- [55] Y.-H. Hsieh, J.-M. Liou, B.-C. Huang, C.-W. Liang, Q. He, Q. Zhan, Y.-P. Chiu, Y.-C. Chen, and Y.-H. Chu, *Adv. Mater.* **24**, 4564 (2012).
- [56] M. W. Finnis, A. Y. Lozovoi, and A. Alavi, *Annu. Rev. Mater. Res.* **35**, 167 (2005).